INTERNATIONAL JOURNAL FOR NUMERICAL METHODS IN FLUIDS, VOL. 25, 973–981 (1997)

SHEAR LAYER INSTABILITY AND ACOUSTIC INTERACTION IN SOLID PROPELLANT ROCKET MOTORS

A. KOURTA[1,2]*

[1] *Institut de Mécanique des Fluides de Toulouse, INPT-URA CNRS 005, Avenue du Prof. Camille Soula, F-31400 Toulouse Cedex, France*

[2] *Centre Européen de Recherche et de Formation Avancée en Calcul Scientifique (CERFACS), 42 Avenue G. Coriolis, F-31057 Toulouse Cedex, France*

SUMMARY

Segmentation of solid propellant rocket motors has been demonstrated to be a source of unpredicted and undesirable pressure and thrust oscillations. Surface discontinuities are the primary cause of these vortex-shedding-driven oscillations, which result from a strong coupling between the shear layer instability and the acoustic motion in the chamber. The analysis of an axisymmetric geometry corresponding to a $\frac{1}{15}$ subscale P230 motor of the Ariane 5 rocket is numerically computed. With a suitable mesh for the viscosity value studied, the aeroacoustics in the chamber is fully described. A coupling between the hydrodynamic instability and the organ-pipe acoustic mode is clearly demonstrated. The mechanism for frequency selection is discussed. © 1997 John Wiley & Sons, Ltd.

Int. J. Numer. Meth. Fluids, **25**: 973–981 (1997)

No. of Figures: 5. No. of Tables: 4. No. of References: 13.

KEY WORDS: aeroacoustics; vortex shedding; space booster; unsteady computation

1. INTRODUCTION

Combustion stability assessment of solid propellant rocket motors used as space boosters is a very interesting research problem. Indeed, segmented solid propellant rocket motors have been reported to exhibit pressure and thrust oscillations, although they were predicted to be stable by classical stability methods. One mechanism that drives pressure oscillations in rocket motors is vortex shedding,[1,2] which can interact with the chamber acoustics to generate pressure oscillations.[3] Owing to the segmented design of solid propellant rocket motors, shear layers induced by surface discontinuities appear and produce vortex shedding. The dipole mechanism involving the interaction of the vortices with an impingement surface is a way for energy to be transferred from the vortex fluctuations to the acoustic field. A strong coupling between the instability of shear flow and the organ-pipe acoustic mode in the chamber modifies the original instability and produces a periodic vortex shedding. The feedback from the acoustic wave provides the control signal for the hydrodynamic instability.

A numerical method well adapted to the description of aeroacoustic interactions inside the combustion chamber of solid propellant rocket motors has been developed by the author and fully

* Correspondence to: A. Kourta, Institut de Mécarique des Fluides de Toulouse, INPT-URA CNRS 0005, Avenue du Prof. Camille Soula, F-31400 Toulouse Cedex, France.

Contract grant number: CNES/ONERA;
Contract grant number: 89/3640

CCC 0271–2091/97/080973–09 $17.50

Received July 1994
Revised January 1997

tested in two previous papers.[4,5] In the last paper,[5] various numerical schemes were tested on three different flow configurations, including the one computed here. The aim of the present paper is to provide a detailed and refined analysis of these interactions in the particular case of the Ariane 5 P230 solid rocket booster and also to evaluate the capacity of this numerical method to handle the aeroacoustic interactions in realistic and complex configurations. The computational domain corresponds to $\frac{1}{15}$ axisymmetric subscale motors for which experimental results exist.[6–8] An experimental investigation,[6] done with various arrangements of inter-segment restrictors, has brought to light the presence of naturally unstable axial modes from the first to the sixth longitudinal mode. Among the four configurations investigated in this experiment, case A corresponds to the Ariane 5 P230 motor. The computation, done with a suitable mesh corresponding to the selected value of viscosity,[4] shows the organization of the flow and the properties of the vortex shedding. Coupling between the instability of the mean flow shear layers and the acoustic motion and resonant interactions are pointed out.

The numerical methodology is presented in Section 2 and the computational results are detailed in Section 3.

2. METHODOLOGY

2.1. Governing equations

The physical model used is the unsteady Navier–Stokes equations without turbulence. It describes the conservation of mass, momentum and total energy. These equations can be written in vector form for the axisymmetric configuration as

$$\frac{\partial W}{\partial t}+\frac{\partial F}{\partial x}+\frac{1}{r}\frac{\partial (rG)}{\partial r}=H, \tag{1}$$

with

$$W=\begin{bmatrix}\rho\\ \rho U\\ \rho V\\ \rho E\end{bmatrix},\qquad F=\begin{bmatrix}\rho U\\ \rho U^2+\sigma_{xx}\\ \rho UV+\sigma_{xr}\\ (\rho E+\sigma_{xx})U+\sigma_{xr}V-\lambda\partial T/\partial x\end{bmatrix},$$

$$G=\begin{bmatrix}\rho V\\ \rho UV+\sigma_{rx}\\ \rho V^2+\sigma_{rr}\\ (\rho E+\sigma_{rr})V+\sigma_{rx}U-\lambda\partial T/\partial r\end{bmatrix},\qquad H=\begin{bmatrix}0\\ 0\\ (1/r)(P+\sigma_{\theta\theta})\\ 0\end{bmatrix},$$

where

$$\sigma_{xx}=P-\mu\left[2\frac{\partial U}{\partial x}-\frac{2}{3}\left(\frac{\partial U}{\partial x}+\frac{1}{r}\frac{\partial rV}{\partial r}\right)\right],$$

$$\sigma_{xr}=\sigma_{rx}=-\mu\left(\frac{\partial U}{\partial r}+\frac{\partial V}{\partial x}\right),$$

$$\sigma_{rr}=P-\mu\left[2\frac{\partial V}{\partial r}-\frac{2}{3}\left(\frac{\partial U}{\partial x}+\frac{1}{r}\frac{\partial rV}{\partial r}\right)\right],$$

$$\sigma_{\theta\theta}=-\mu\left[2\frac{V}{r}-\frac{2}{3}\left(\frac{\partial U}{\partial x}+\frac{1}{r}\frac{\partial rV}{\partial r}\right)\right].$$

To close this set of equations, the pressure is related to the other state variables ρ and T by the law of state for perfect gases. Here (U, V) is the velocity field, ρ, T, P and E are the density, temperature, pressure and total energy respectively and μ and λ are the viscosity and thermal diffusivity respectively.

2.2. Numerical method

The numerical method used is a finite volume version of the explicit MacCormack scheme.[5,9,10] It consists of a predictor–corrector approach. For each time step, forward or backward approximations are used for the inviscid part and central differences for the viscous terms. The two steps of the scheme can be written as follows: for the predictor step,

$$\Delta W^n = -\Delta t\left(\frac{\partial F^n}{\partial x} + \frac{1}{r}\frac{\partial rG^n}{\partial r} - H^n\right),$$
$$\overline{W^{n+1}} = W^n + \Delta W^n;$$

for the corrector step,

$$\Delta W^{n+1} = -\Delta t\left(\frac{\partial \overline{F^{n+1}}}{\partial x} + \frac{1}{r}\frac{\partial r\overline{G^{n+1}}}{\partial r} - \overline{H^{n+1}}\right),$$
$$W^{n+1} = \tfrac{1}{2}(W^n + \overline{W^{n+1}} + \Delta W^{n+1}).$$

Here $\Phi^n = \Phi(W^n)$, where Φ can be F, G or H.

The predictor step yields intermediate values for the variables at each mesh point, using one-sided differences to approximate the first derivatives. The corrector step corrects the former approximation with opposite one-sided differences for the first derivatives. At each mesh point (i, j) the applied MacCormack scheme is then given by: for the predictor step,

$$\Delta W^n_{i,j} = \Delta t\left(\frac{D_+F^n_{i,j}}{\Delta x} + \frac{1}{r}\frac{D_+rG^n_{i,j}}{\Delta r} - H^n_{i,j}\right),$$
$$\overline{W^{n+1}_{i,j}} = W^n_{i,j} + \Delta W^n_{i,j};$$

for the corrector step,

$$\Delta W^{n+1}_{i,j} = \Delta t\left(\frac{D_-\overline{F^{n+1}_{i,j}}}{\Delta x} + \frac{1}{r}\frac{D_-r\overline{G^{n+1}_{i,j}}}{\Delta r} - \overline{H^{n+1}_{i,j}}\right),$$
$$W^{n+1}_{i,j} = \tfrac{1}{2}(W^n_{i,j} + \overline{W^{n+1}_{i,j}} + \Delta W^{n+1}_{i,j}).$$

Here D_+ and D_- denote right-sided and left-sided differences respectively.

In order to restore the second-order accuracy, a cycle is set up on four iterations by reversing the backward and forward operators between the two steps and alternating them between the longitudinal and axial directions.

The scheme is second-order-accurate in time and space. In the present numerical code it is also possible to use an implicit method based on a Gauss–Seidel line relaxation technique or a flux-splitting technique, but in order to compute an unsteady flow, it has been shown that computation without these options is more accurate and practical, because both these techniques induce damping effects.[5]

2.3. Computational domain

The test case computed is based on a segmented motor model. This case is axisymmetric and requires a multiblock technique. It represents configuration A of the ONERA LP3 experiment. The chosen sequence corresponds to 20 mm of burning propellant, for which an important instability at the third mode (900 Hz) was observed.[6–8] The meshes are designed by ONERA.[8] Three mesh levels have been tested for this study. The medium one is obtained from the fine one by removing every second point in both directions and the coarse one is obtained from the medium one in the same way. The geometry and the mesh are presented in Figure 1. The configuration is divided into five blocks. In a previous study[4] the results for different viscosity values (laminar viscosity (μ_{lam}), $80\mu_{\text{lam}}$ and $400\mu_{\text{lam}}$) have shown a mesh dependency. At $80\mu_{\text{lam}}$ it is necessary to use the finer mesh (Table I) to obtain a good prediction. As will be seen later, this grid size is suitable for resolving the boundary layer at the second diaphragm where the origin of instability is located. Vuillot *et al.*,[8] have encountered a cell Reynolds number limitation at the second diaphragm (no-slip wall). Hence they define a viscosity limit. For the fine grid the observed limitation is $\mu > 50\mu_{\text{lam}}$. Also, in the range $50\mu_{\text{lam}} \leqslant \mu < 200\mu_{\text{lam}}$ the solutions obtained with the fine mesh are approximately the same. Thus, in view of these results and in order to verify the limit observed by Vuillot *et al.*[8] necessary to capture the boundary layer that develops along the second diaphragm (minimum of six grid points), we chose the viscosity of $80\mu_{\text{lam}}$ to perform computations on the fine mesh.

2.4. Boundary and initial conditions

The boundary conditions imposed are given in Table II. No-slip conditions are imposed on inert walls where the velocity and normal pressure gradient are equal to zero. On injecting walls the mass flow rate, the temperature and zero tangential velocity are specified. For supersonic outflow, classical first-order extrapolations are used.

For initial conditions, computations are started from rest.

2.5. Physical values

The physical values used are given in Table III, where ρ_{p} is the propellant density, V_{c} is the propellant burning rate, $\dot{m}$ is the injection mass flow rate $(\rho v)_{\text{inj}}$, T_{f} is the flame temperature, a is the

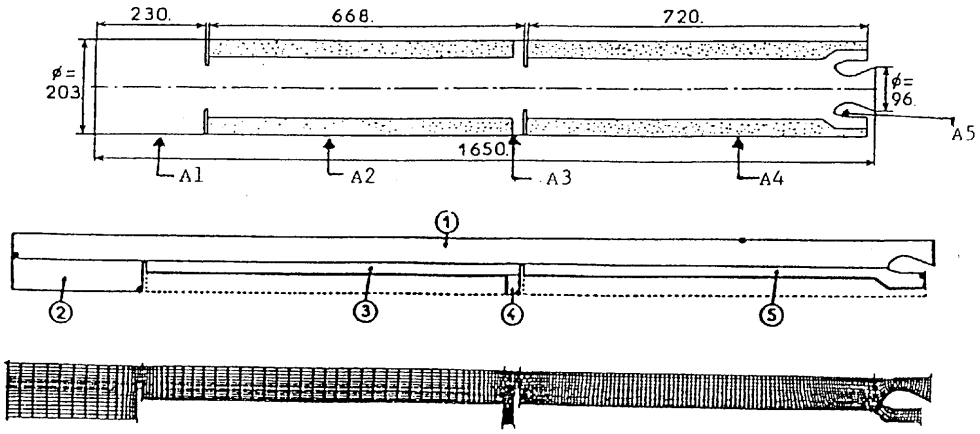

Figure 1. Computational domain

Table I. Mesh size

Block	1	2	3	4	5
Mesh	821×37	61×37	217×21	37×37	529×21

Table II. Boundary conditions

Head end	Aft end	Internal side	External side[a]
No slip	Supersonic outflow	Symmetry	A2, A4: injecting wall A1, A3, A5: no slip

[a] A1, A2, A3, A4 and A5 are defined in Figure 1.

Table III. Physical values (SI units)

ρ_p	V_c	$\dot{m}$	T_f	a	R	μ_{lam}	γ	Pr
1640	$7{\cdot}38 \times 10^{-3}$	12·1032	2700	1061·27	340·53	$8{\cdot}1 \times 10^{-5}$	1·225	1

speed of sound. R is the perfect gas constant, μ_{lam} is the dynamic viscosity, γ is the ratio of specific heats and Pr is the Prandtl number.

3. COMPUTATIONAL RESULTS

The velocity profile at the second diaphragm is plotted in Figure 2. Ten computation points are present in the boundary layer. In this case a small recirculating zone characterized by negative velocities is detected. This separation is not detected when coarser meshes or higher viscosity values are used, but it can be helpful to explain the nature of the interaction between the flow and the acoustic wave. Figure 3 shows the iso-vorticity at various times. The formation of the vortex can be seen and a pairing mechanism takes place. The new vortex resulting from the pairing mechanism is absorbed by the nozzle. Various vortices of different sizes exist in the flow and complex non-linear

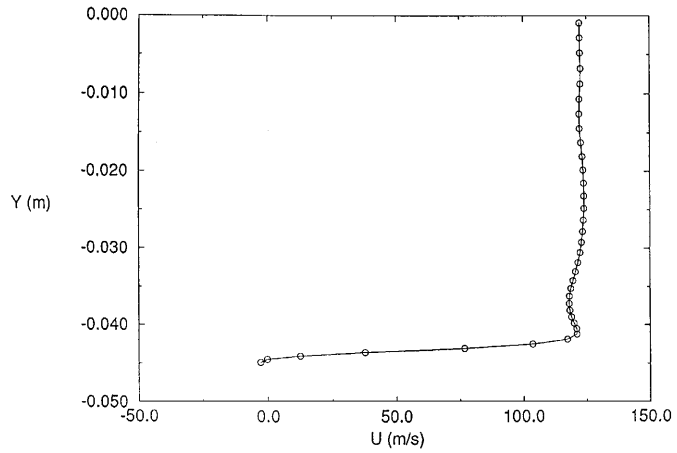

Figure 2. Velocity profile at second diaphragm

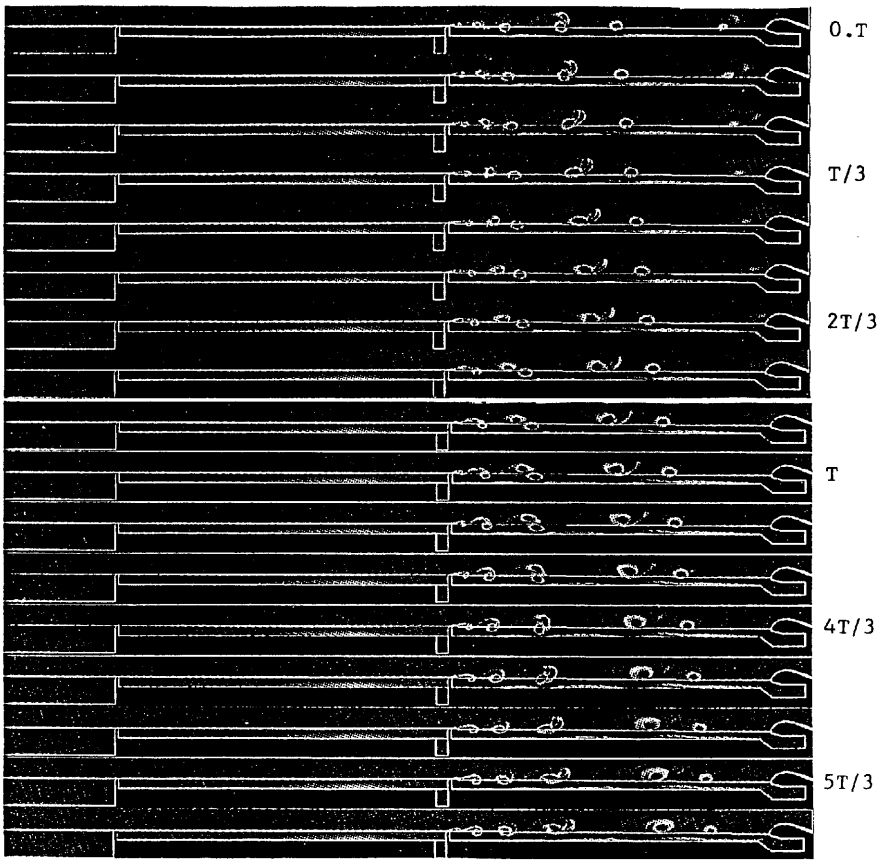

Figure 3. Iso-vorticity contours

interactions can appear. The signals obtained are not monochromatic and contain complex phenomena. Figure 4 presents the time evolution of the thrust and shows that even though an organized frequency seems to be apparent, the signal is quite complex, involving various frequency interactions. In Table IV are given the mean values and amplitudes of the exit mass flow rate ($\dot{m}_e$), the thrust (Th), the head-end pressure (P_{he}), the aft-end pressure (P_e^a), the pressure at the first diaphragm (P_{I1}) and the pressure at the second diaphragm (P_{I2}). The amplitudes of the pressure oscillations are higher in the rear part of the chamber, between the second diaphragm and the throat (P_{I2}, P_{ae}). The ratios of the pressure oscillations to the mean values are small (P_{he}, 0·2%; P_{ae}, 0·6%, P_{I1}, 0·16%; P_{I2}, 0·4%). However, the thrust oscillations are relatively more significant (2·5%), showing that the accumulation of organized oscillations has a great effect on the integrated forces. Hence the thrust is more perturbed by the aeroacoustic interaction than is the pressure.

The spectra exhibit many peaks, as can be observed in Figure 5. Frequencies detected by experiments are predicted. The axial evolution of the spectra provides information on the non-linear vortex interaction. Near the shear layer origin at the first position (Figure 5a) a dominant peak is observed at 1800 Hz. This frequency corresponds to the sixth acoustic mode of the chamber. With the help of the time evolution of the iso-vorticity (Figure 3) it has been observed that this frequency

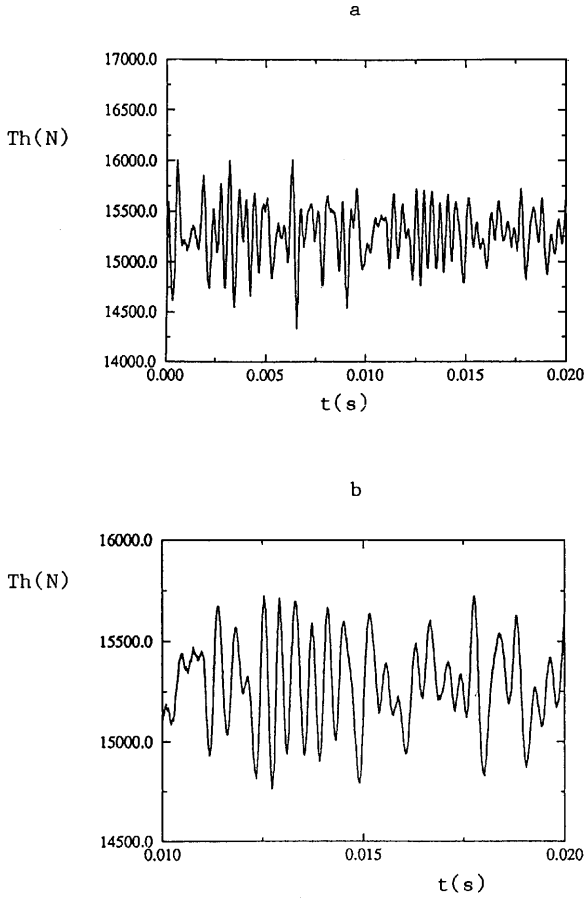

Figure 4. Time history of thrust: a, complete history; b, 'zoom-in' ensemble

corresponds also to the initial roll-up process. Thus the vortex shedding is driven by the sixth acoustic mode of the chamber. The selection mechanism of the vortex-shedding frequency is related to the shear at the origin of the mixing layer near the second diaphragm. The intensity of this initial shear defines the selected frequency corresponding to the critical mixing layer one. In fact, when the viscosity is equal to $400\mu_{\text{lam}}$, the vortex-shedding frequency corresponds to the third mode (900 Hz)[4] and in this case no separation has been detected. In the present case, owing to the existence of separation, the initial shear is different and consequently the natural vortex-shedding frequency is different. Peaks at the fourth and ninth modes of the chamber (1200 and 2700 Hz) and at the first acoustic mode of the head-end cavity (2300 Hz) are also present in the spectrum. At the second position (Figure 5b) the dominant peak corresponds to 900 Hz. Hence at this position the pairing of

Table IV. Mean values and amplitudes (SI units)

	$\dot{m}_e$	Th	P_{he}	P_{ae}	P_{I1}	P_{I2}
Mean	7.191	15280	4305044	4221451	4304996	4290768
Amplitude	0.03	380	9085	26916	6813	15200

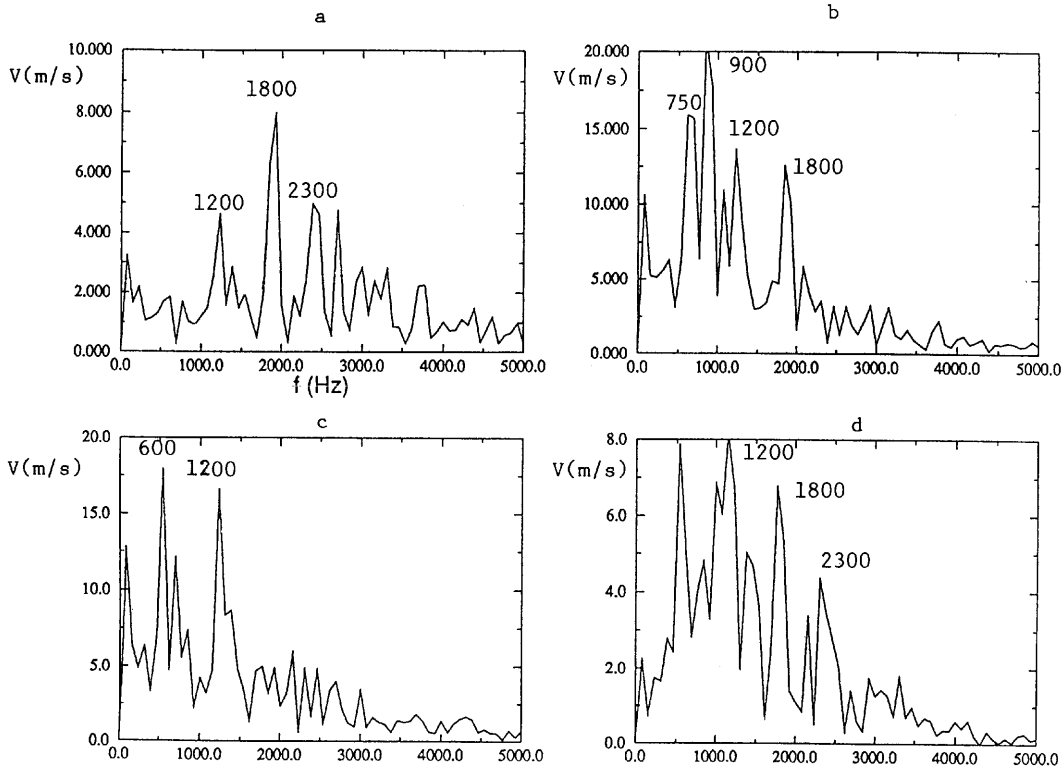

Figure 5. Spectra of V-component in mixing layer: a, $x/L = 0{\cdot}575, r/L = 0{\cdot}025$; b, $x/L = 0{\cdot}63, r/L = 0{\cdot}025$; c, $x/L = 0{\cdot}745, r/L = 0{\cdot}025$; d, $x/L = 0{\cdot}86, r/L = 0{\cdot}026$

two vortices emitted at 1800 Hz occurs. Peaks at 750, 1200 and 1800 Hz are also present in this spectrum. The peak at 750 Hz corresponds to the first acoustic mode of the cavity between the second diaphragm and the throat. The peak at 600 Hz, corresponding to the pairing of three vortices emitted at 1800 Hz, is detected at the third position (Figure 5c). The peak at 1200 Hz is also important in this position. At the last position (Figure 5d) the spectrum exhibits the following peaks with decreasing intensities: 1200, 600, 1800, 900, 750, 1500, 1200 and 450 Hz. Thus the axial evolution of the shear layer is dominated by the pairing of vortices linked to the acoustic modes of the chamber. Moving downstream, peaks corresponding to the pairing of two (900 Hz), three (600 Hz) and four (450 Hz) vortices emitted at 1800 Hz occurs. In fact, the pairing of vortices is directly related to the development of subharmonics.[11,12] The pairing mechanism constitutes one of the most striking features in the mixing layer dynamics[12,13] as it is related to the complex non-linear self-coupling of vorticity modes under acoustic control. It can be noticed that all frequencies detected are not necessarily related to vortices. Acoustic wave frequencies of the subcavities are detected that do not control the vortex mechanism. Frequencies arising from non-linear hydrodynamic interaction[12] can also be observed (1200 Hz = 1800 − 600 Hz, 2700 Hz = 1800 + 900 Hz).

4. CONCLUSIONS

The present study consists of the analysis of the aeroacoustics in a solid propellant rocket motor. The interaction between the hydrodynamic instability and the acoustics has been described. Vortex

shedding and pairing result from this strong interaction. The vortex-shedding frequency corresponds to the sixth chamber acoustic mode (1800 Hz). Subharmonics exhibited by the spectra are related to the pairing (900 and 600 Hz) or to the non-linear hydrodynamic interaction (1200 Hz). Acoustic modes of the aft-end (750 and 1500 Hz) and head-end (2300 Hz) cavities are also detected. Thus the vortex shedding is controlled by the acoustics of the chamber excited by vortical structures in the shear layer. We also pointed out that the thrust is more affected by the oscillation than is the pressure.

ACKNOWLEDGEMENTS

This work has been supported by CNES/ONERA contract 89/3640. I would like to thank Dr. H. C. Boisson for valuable comments.

REFERENCES

1. G. A. Flandro and H. R. Jacobs, 'Vortex generated sound in cavities', *AIAA Paper 7301014*, 1973.
2. G. A. Flandro, 'Vortex driving mechanism in osillatory rocket flows', *J. Propuls. Power*, **3**, 206–214 (1986).
3. F. E. C. Culick and K. Magiawala, 'Excitation of acoustic modes in a chamber by vortex shedding', *J. Sound Vibr.*, **64**, 455–457 (1979).
4. A. Kourta, 'Vortex shedding in solid rocket motors', *AIAA Paper 95-0727*, 1995.
5. A. Kourta, 'Acoustic–mean flow interaction and vortex shedding in solid rocket motors', *Int. j. numer. method fluids*, **22**, 449–465 (1996).
6. M. Prevost, J. C. Traineau, F. Vuillot and C. Caugant, 'Experiments on 1/15 subscale segmented motors', *Colloq. CNES-ONERA 6(1–30)*, 1992.
7. N. Luppoglazoff and F. Vuillot, 'Simulation numérique 2-D instationnaire de l'écoulement dans une maquette à l'echelle 1/15eme du propulseur d'Ariane 5: première comparison avec l'expérience', *Colloq. CNES-ONERA 14(1–16)*, 1992.
8. F. Vuillot, J. C. Traineau, M. Prevost and N. Luppoglazoff, 'Experimental validation of stability assessment methods for segmented solid propellant motors', *AIAA Paper 93-1883*, 1993.
9. R. MacCormack, 'A numerical method for solving the equations of compressible viscous flow', *AIAA Paper 81-0110*, 1981.
10. R. MacCormack, 'Current status of numerical solutions of the Navier–Stokes equations,' *AIAA Paper 85-0032*, 1985.
11. C. M. Ho and P. Huerre, 'Perturbed free shear layers', *Ann. Rev. Fluid Mech.*, **16**, 365–424 (1984).
12. A. Kourta, H. C. Boisson, P. Chassaing and H. HaMinh, 'Nonlinear interaction and transition to turbulence in the wake of a circular cylinder', *J. Fluid Mech.*, **181**, 141–161 (1987).
13. A. Kourta, M. Braza, P. Chassaing and H. HaMinh, 'Numerical analysis of a natural and excited two-dimensional mixing layer,' *AIAA J.*, **25**, 279–286 (1987).

